Advanced Composites and Hybrid Materials (2024) 7:65
https://doi.org/10.1007/s42114-024-00877-8

RESEARCH

3D macroporous $Ti_3C_2T_x$ MXene/cellulose nanofibre/rGO hybrid aerogel electrode with superior energy density

Xiaoyu Bi[1] · Yang Shi[1] · Shengbo Ge[1] · Ben Bin Xu[2] · Xia Li[3] · Ximin He[4] · Runzhou Huang[1]

Received: 30 October 2023 / Revised: 18 February 2024 / Accepted: 20 March 2024 / Published online: 1 April 2024

Abstract

Reduced graphene oxide (rGO) and MXene have garnered significant attention due to their exceptional pseudocapacitance and electrical conductivity that are viable in energy storage applications. Nevertheless, the challenge of self-restacking between the 2D material surfaces and the tendency of MXene to oxidise has posed obstacles to their further utilisation. This prompted researchers to use cellulose nanofibre (CNF) as a prospective "bridge" to connect the two materials. This approach has been shown to prevent MXene from oxidising while facilitating GO conversion into rGO via reduction. Consequently, 3D macroporous $Ti_3C_2T_x$ MXene/cellulose nanofibres/reduced graphene oxide (MCG) aerogels have been successfully prepared. A breakthrough in solving the self-stacking problem and creating a sensibly designed 3D macroporous electrode structure has yielded excellent electrochemical capabilities for MCG aerogel electrodes. Specifically at 1.0 mW cm^{-2} power density, these electrodes have demonstrated an outstanding performance in 5000 cycles with 79.4% retention rate, favourable areal specific capacitance of 671 mF cm^{-2} and unparalleled energy density of 60.9 mWh cm^{-2}. Overall, this study offers significant perspectives on the possible uses of 2D materials, especially in terms of adjusting their structure and functionality.

Keywords Aerogel · MXene · Cellulose nanofibre · rGO · VC · Supercapacitor

1 Introduction

There are many potential application prospects for supercapacitors, which have sparked an attractive interest due to their energy storage capabilities [1]. These devices possess long life cycle, rapid discharging and charging speed and superior power density [2, 3]. However, the incorporation of binders such as conductive agents (e.g. carbon black), polyvinylidene fluoride and polytetrafluoroethylene into common electrodes has a notable impact on the active substance mass ratio in electrodes. As a result, reactive sites are not exposed to their full potential, which compromises the efficiency of ion diffusion and reduces the specific capacitance [4]. In contrast, lightweight devices require a strong bond between the electrode material and substrate or a binder-free, self-supporting electrode material. Despite the benefits of this type of electrode for practical applications, fabrication still poses several challenges, particularly in achieving high capacitances and reliable mechanical strength.

MXene has received substantial interest in the field of energy storage and electromagnetic shielding research because of its profound pseudocapacity, surface-terminating moieties and metallic conductivity that can be modified [5, 6]. The structure of this material is produced during the MAX phase by meticulously eliminating the Al layer, resulting in a two-dimensional lamellar framework expressed as $M_{n+1}X_nT_x$, in which T_x represents a surface functional moieties (-O, -F, -OH) [7]. Hydrophilicity is imparted to the material by the

✉ Shengbo Ge
geshengbo@njfu.edu.cn

✉ Xia Li
lixia1069@ujs.edu.cn

✉ Runzhou Huang
runzhouhuang@njfu.edu.cn

1 Co-Innovation Center of Efficient Processing and Utilization of Forest Resources, College of Materials Science and Engineering, Nanjing Forestry University, Nanjing 210037, China

2 Department of Mechanical and Construction Engineering, Northumbria University, Newcastle Upon Tyne NE1 8, UK

3 School of Environment and Safety Engineering, Biofuels Institute, Jiangsu University, Zhenjiang 212013, China

4 Department of Materials Science and Engineering, University of California, Los Angeles (UCLA), Los Angeles, CA 90095, USA

abundant surface functional groups that enable it to disperse into an aqueous solution that is homogeneous and stable. The properties of this material are especially advantageous for subsequent treatments like vacuum filtering, spin coating and freeze drying [8, 9]. These surface-rich functional groups are also conducive to combining with other ingredients via hydrogen bonding, thus avoiding the utilisation of binders, which allows for the preparation of self-supporting electrodes. The rigid, large sheet geometry enables the assembly of 3D structures with the other 1D or 2D materials. Meanwhile, the advantages of their self-lightness, high conductivity(8000 S cm^{-1}) and higher theoretical specific capacitance (1200 F g^{-1}) can also be maintained [10]. Compared to other 2D materials, the favourable hydrophilicity of MXene also facilitates the formation of a more uniform and continuous interface between the electrode material and the electrolyte, which is beneficial for a higher ratio of pseudocapacitance contribution in aqueous-based energy storage system.

However, the obvious advantages are always accompanied by problems that are difficult to handle. One of the most common drawbacks of 2D materials is the irreversible surface-to-surface self-stacking that occurs because of hydrogen bonding within surface functional groups plus the van der Waals interactions. This phenomenon could severely affect electron transport kinetics and reduce the active surface area available for pseudocapacitive reactions on the surface, resulting in compromised electrochemical performance [11, 12]. Among the most promising techniques for overcoming this limitation is assembling 2D components to create 3D structures [13]. The advantages of this approach are that it reveals additional reaction sites for use, expands the specific surface area of the material and facilitates the relocation of electrolyte ions within the microporous structure [14, 15]. Recently, considerable interest has been attracted towards the integration of carbon materials like graphene and porous carbon with $Ti_3C_2T_x$ MXene to prepare high-performance hybrid electrode materials [16–18]. Reduced graphene oxide (rGO) represents one such material that possesses outstanding electrical conductivity, abundant in functional groups containing oxygen coupled with excellent hydrophilicity and profound specific surface area. These properties make it particularly easy to be transformed into 3D macroscopic hybrid electrode materials utilised in energy storage tools [19, 20]. MXene/rGO composite aerogels have been prepared at room temperature using a simple self-assembly method developed by Shao et al. The anisotropic three-dimensional (3D) porous aerogel exhibited favourable cyclic compression properties at 10-kg loading capacity and high strength (~ 16 MPa). Moreover, this electrode exhibits an exceptional electrochemical performance of 233 F g^{-1} at 1 A g^{-1} with 91% cycling performance after 10,000 cycles as a self-supporting supercapacitor electrode [21]. But, there is still obvious self-stacking phenomenon that can be observed, which shows a huge hinder for further improving their capacitance. Overall, the findings demonstrate the merits of 3D hybrid electrodes for applying in energy storage field.

As a versatile nanomaterial, cellulose nanofibre (CNF) represents an encouraging choice due to its abundant, inexpensive, green, biodegradable, and renewable characteristics and its high mechanical strength and aspect ratio [22, 23]. When combined with MXene or rGO, CNF can form a stable colloidal suspension because of the electrostatic repulsion between positive charge of CNF surface and negative charge of MXene or rGO nanosheet, which can obtain a uniform hydrogel as a consequence of hydrothermal processing. Water removal by lyophilisation results in an aerogel with exceptionally extended channels among the lamellar frameworks inside. Charge diffusion and ion transport are crucial aspects of maintaining electrode-specific capacitance [21, 24]. The use of cellulose nanofibre (CNF) as a binder and intercalating agent enables effective utilisation of the unique surface area of 2D lamellar materials while preserving their complete 3D structure. This approach ensures full exploitation of the advantages offered by 2D materials and is a promising avenue for future research and development in this field. In a recent study, Cai et al. employed functionalised cellulose nanocrystals as structural modifiers in conjunction with MXene 2D nanosheets via polyurethane to direct the ice template process, yielding multi-layered nanostructured aerogel electrodes with interconnected porous channels. The MXene aerogels exhibited high ion channels with low bending topology, resulting in exceptional electrochemical characteristics, including an energy density of 38.5 μWh cm^{-2}, capacitance of 225 F g^{-1}, and 86.7% cycling capability after 4000 cycles [25]. In spite of this, MXene typically undergoes oxidation and even degradation due to high-temperature hydrothermal treatments [26, 27]. Therefore, selecting a suitable intermediate as an additive that avoids the oxidation of the main pseudocapacitive contributor, MXene, and does not interfere with the binding properties to other agents is of utmost priority in the next investigations.

In this study, a new MXene/CNF/rGO composite aerogel (named MCG-X, in which X refers to the MXene content in the hybrid hydrogel) was synthesised via a combined hydrothermal and freeze-drying technique. The surface of cellulose nanofibres (CNF) contains a plethora of hydroxyl functional groups which act as intermediates to combine functional groups containing oxygen present on the surfaces of both graphene oxide (GO) and MXene through intense hydrogen bonding. This has led to creating a more solid 3D macroporous framework that enhances electrode conductivity. The L-ascorbic acid (VC) added during fabrication eliminates the functional groups containing oxygen from MXene surface. Consequently, it reduces or even prevents the oxidation of MXene during hydrothermal treatment. The findings suggest that CNF significantly prevents the accumulation of rGO and MXene and modulates the electrode structure.

Moreover, the surface pseudocapacitance reactivity is significantly improved. The MCG-2 aerogel electrode exhibits an area-specific capacity of 671 mF cm^{-2} at 5 mV s^{-1} and maintains 102 mF cm^{-2} at 100 mV s^{-1}. The symmetrical device assembled using this technique demonstrates a profound area capacitance of 662 mF cm^{-2} at 5 mV s^{-1}. Notably, the 3D macroporous MCG-2 symmetrical device exhibits extraordinary cycling stability, retaining 79.4% capacitance at 20 mA cm^{-2} after 5000 cycles.

2 Materials and methods

2.1 Research materials

Lithium fluoride (LiF, 99%), hydrochloric acid (HCl, 35–38%), L-ascorbic acid (VC), and sulphuric acid (H_2SO_4) were procured from Aladdin Reagent Co., Ltd. The layered ternary carbide (Ti_3AlC_2, MAX) powders were manufactured by FoShan XinXi Technology Co., Ltd. in Guangzhou, China. Graphene oxide (GO) procurement was facilitated through Qingdao Graphite Company in Qingdao, China. Lastly, cellulose nanofibres (CNFs) at a concentration of 2.5 wt% were supplied by Zhong Shan NanoFC Co., Ltd., based in Guangdong, China.

2.2 Synthesis of $Ti_3C_2T_x$ colloidal suspension

In fabricating $Ti_3C_2T_x$, Al species from the MAX phase were selectively etched. The process began by dissolving 2.8 g of LiF powder in 40 mL of HCl (9 M) and stirring at around 25 °C for 20 min to create the etching solution. Then, 2 g of Ti_3AlC_2 powder (400 mesh) was gradually added to the LiF/HCl solution. The suspension was stirred using a magnetic method for 48 h at 35 °C. Afterward, it was washed extensively with deionised water and then centrifuged (at 3500 rpm for 8 min) until the pH 6. After being collected, the deposit was mixed with deionised water and subjected to sonication for 25 min. This process was carried out in an ice-water bath with argon gas bubbles present beneath the liquid surface. After being centrifuged for 40 min at 3500 rpm, a dark green supernatant was obtained, resulting in a $Ti_3C_2T_x$ suspension that had been delaminated (with a concentration of approximately 6 mg/mL).

2.3 Synthesis of $Ti_3C_2T_x$/cellulose nanofibre/rGO hybrid aerogel electrode

The preparation of MXene/CNF/RGO (MCG) aerogel involved a series of steps. Initially, the GO and CNF substances were scattered in water that had been deionised through sonication for 1 h. And a homogeneous suspension was produced by adding MXene (6 mg mL^{-1}) dropwise to a mixture of GO (3 mL, 8 mg mL^{-1}) and CNF (4 mL, 6 mg mL^{-1}) colloidal suspensions. The suspension was then stirred in an argon atmosphere for approximately 30 min. An array of MCG aerogels was synthesised with varying MXene mass ratios to investigate the aerogel properties. All aerogels were produced following the aforementioned procedure, and the detailed contents of the various materials and chemicals used are listed in Table S1. Subsequently, L-ascorbic acid (VC, 50 mg) was added to the colloidal suspension; then, it was stirred for half an hour and ultrasonicated in an ice bath for 10 min. Thirdly, the suspension was isolated in a 20-mL vial for 300 min at 90 °C. The MCG hydrogels were extracted and purified through dialysis in deionised water until the supernatant pH (around neutral pH). After freeze-drying, the as-prepared MCG hydrogel was transformed into MCG aerogel. Finally, after being annealed under argon at a temperature of 600 °C for a duration of 60 min, the MCG aerogel underwent pressing at 5 MPa for 300 s, resulting in a set of binder-free MCG aerogel electrodes. It should be highlighted that the ascorbic acid present in the hybrid gel was eliminated during the annealing process.

2.4 Material characterisations

The microstructure and morphology of the specimens were analysed utilising a field-emission scanning electron microscope (FE-SEM, Regulus 8100) along with energy-dispersive spectroscopy (EDX), JEM-2100 high-resolution transmission electron microscope (HR-TEM) and JEM-1400 transmission electron microscopy (TEM). Additionally, the samples were characterised using Fourier transform infrared (FTIR) spectroscopy on a VERTEX 80 V FTIR spectrometer at room temperature. The wavenumber range of 500–4000 cm^{-1} was used with a resolution of 4 cm^{-1}. The diffractometer was set to scan within a 2θ range of 3–80° at 0.05° min^{-1}. To determine the chemical structure of the samples, an X-ray diffractometer (XRD, Ultima IV) was utilised. The XRD used a radiation source of Cu Kα at 40 kV and 30 mA.

X-ray photoelectron spectroscopy (XPS) was utilised to detect the surface chemical compositions and bonding states. The Al Kα X-ray source was set at 15 kV, 10 mA and 160 eV for the survey scan mode and 40 eV for the high-resolution scan mode, such as C 1 s and Ti 2p. The chemical bonding states were analysed using CASAXPS software by deconvoluting high-resolution spectra. Gas (N_2) adsorption/desorption isotherms were performed using the Autosorb-iQ2-MP (Quantachrome) in order to examine the porosity of the aerogel. The Brunauer–Emmett–Teller method was utilised to evaluate the specific surface area (SSA), while the density functional theory (DFT) was used to assess the pore size distribution.

2.5 Electrochemical characterisations

The CHI 760E electrochemical workstation from Chenhua, Shanghai, China, was used to conduct electrochemical testing. The electrochemical performance of each electrode was evaluated using a three-electrode setup with 1 M H_2SO_4 as the aqueous electrolyte. The counter electrode was made of glassy carbon, and the reference electrode was Ag/AgCl in saturated KCl. The electrochemical functionality of the supercapacitor was assessed by a CR2032 coin-type cell. The coin-type cell was assembled in the air with MCG aerogel, 1 M H_2SO_4 aqueous solution, and Whatman GF/A glass microfibre filter as electrodes, electrolyte, and separator, respectively. Electrochemical impedance spectroscopy (EIS), galvanostatic charge–discharge (GCD) and cyclic voltammetry (CV) were applied to study the electrochemical properties of individual electrodes and symmetric devices. The open-circuit potential EIS test was performed with a 5-mV amplitude and a frequency range of 10^{-2} to 10^{3} kHz. To evaluate its long-term cycling stability, the GCD test was conducted for 5000 cycles with a current density of 20 mA cm^{-1}.

To determine the specific capacitance of individual electrodes, the discharge portion of cyclic voltammetry (CV) curves was analysed using the provided equations [28]:

$$C_a = \frac{\int IdV}{av\Delta V} \tag{1}$$

where C_a is the areal capacitance (mF cm^{-2}), I is the current (mA cm^{-2}), ΔV is the potential window (V), a is the area of one electrode (cm^{-2}) and v is the scan rate (mV s^{-1}), respectively.

The gravimetric capacitance (C_g) was tabulated based on the equation:

$$C_g = \frac{aC_a}{m} \tag{2}$$

where m is the amount of active materials (g).

Calculations of symmetric device capacitance were derived from the discharge segment of cyclic voltammetry (CV) curves. The equations utilised were for determining both areal capacitance and gravimetric capacitance [29].

$$C_A = \frac{\int IdV}{Av\Delta V} \tag{3}$$

$$C_G = \frac{AC_A}{G} \tag{4}$$

where A is the geometric area of the electrode material (cm^{-2}), and G is the total mass of positive and negative electrodes (g).

Calculations were conducted to determine the gravimetric energy density (μWh·cm^{-2}) and gravimetric power density (mW cm^{-2}) of an asymmetric supercapacitor, using the equations provided [30]:

$$E = \frac{1}{7.2}C_a V^2 \tag{5}$$

$$P = \frac{3600E}{\Delta t} \tag{6}$$

where Δt is the discharge time (s).

3 Results and discussion

A three-dimensional macroporous MCG hydrogel was prepared using the bridge-linking effect of CNF via the self-assembly mechanism happened between graphene nanosheets and $Ti_3C_2T_x$ MXene; meanwhile, the VC offered antioxidant support (for MXene) and reduction effect (for GO) for the hydrogel at 90 °C within 5 h (Fig. 1). During the preparation process, CNF served as an improving and crosslinking agent, while VC was adopted as a reducing agent to modify the MXene surface functional moieties, thus hindering oxidation and reducing graphene oxide to rGO. $Ti_3C_2T_x$ Mxene nanosheets were synthesised via specific etching and ultrasonic delamination of the Al atomic layer in the MAX (Ti_3AlC_2) precursor by conventional methods. Consequently, steady monolayer MXene colloidal dispersions were successfully obtained. It is worth noting that protecting MXene from being oxidised in the whole synthesis process should never be ignored, as Ti_3AlC_2 is the domestic material that provide pseudocapacitance for the energy strorage system. And that was exactly why L-ascorbic acid was added into the mixture before heating treatment. On the other hand, the superior conductivity that are provided by rGO could also compensate the inadequate electronic conductivity of CNF; otherwise, the insulating nature of CNF would cause some consequences. Additionally, abundant hydroxyl groups on CNF surfaces facilitated the interaction among rGO nanosheets and functional moieties containing oxygen on the MXene surfaces via hydrogen bonding. At the same time, the uniformly distributed electrostatic charge on the cellulose surface is a decisive factor for the homogeneous dispersion of the colloidal solution of MXene and rGO, which ensures the formation of a continuous and homogeneous 3D conductive network during the connecting process. This interaction resulted in the formation of 3D macroporous hybrid hydrogels with reliable electrochemical performance. Thus, it ensures greater energy density than conventional capacitors and improved power density compared to batteries.

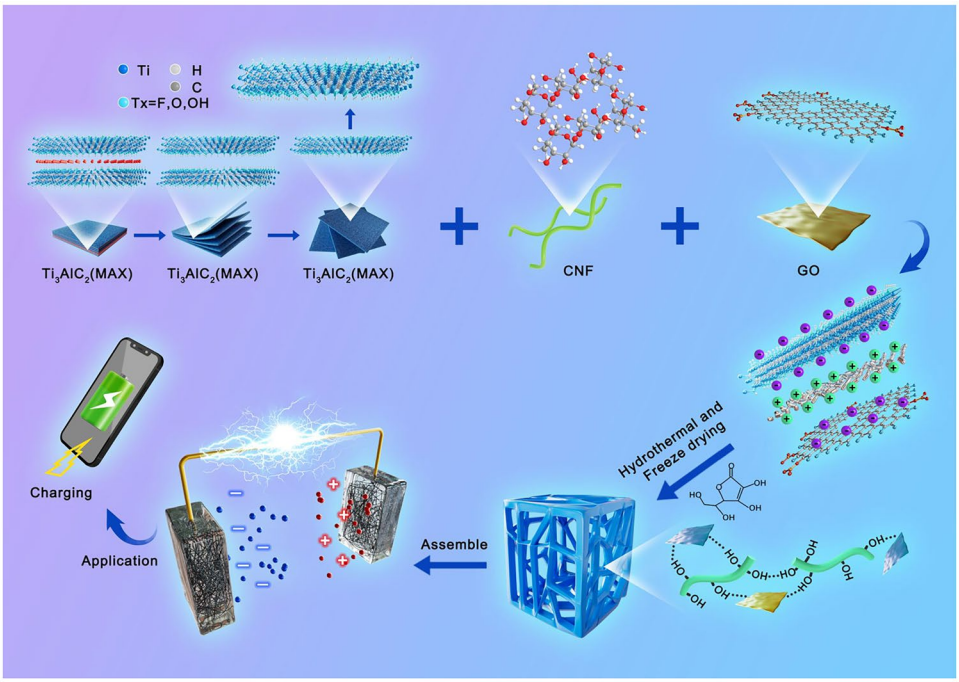

Fig. 1 Construction procedures for the 3D macroporous MCG hybrid aerogel

3.1 Physical and chemical characteristics of $Ti_3C_2T_x$/CNF/rGO hybrid aerogels

Figure 2 a and b showcase digital images of MCG series aerogels containing varying amounts of MXene. These photographs demonstrate the remarkable lightweight nature of MCG aerogel. The material comfortably rests on a flexible leaf, while even a small drop of water can easily bend the leaf. The diameter and height of several aerogels are consistent, measuring approximately 2 cm and 0.9 cm, respectively, leading to a calculated volume of roughly 2.83 cm^{-3}. The densities of various aerogels have been determined through weight measurements. Different amounts of MXene result in a difference in density, which ultimately affects the overall quality of the aerogel due to a lack of binder content [31]. The microscopic structure and morphology of the composite MCG aerogels were visualised using electron microscopies (i.e. FE-SEM and TEM). The differing morphologies of MXene and rGO were distinguishable, with rGO displaying more wrinkled structures due to its relative softness. In contrast, the more rigid MXene nanosheets showed relatively smooth 2D planar morphologies, as demonstrated in Fig. 2c and d [32]. Furthermore, Fig. 2c and d show that CNFs with diameters of about 5–8 nm were also present. The CNF acted as a connecting bridge with constant content, but the variation in MXene percentage resulted in the observed density variation.

Upon analysing high-resolution TEM, it is apparent that parallel lattice stripes exist. XRD measurements have demonstrated that MXene and rGO exhibit significantly different lattice spacings. Specifically, MXene and rGO lattice spacings are 1.55–1.57 nm and 0.33 nm, respectively. This serves as compelling evidence that the hybrid aerogel effectively incorporates MXene and rGO. Interestingly, the lattice spacing of MXene (1.55–1.57 nm) is noticeably larger than that of pure MXene (only 0.25–0.27 nm). This leads to the assumption that the stacking phenomenon is highly attenuated, thereby exposing a more specific surface area [33, 34]. This is made possible by the mutual self-assembly among rGO, CNF and MXene, which create a more rational structural space and enhances ion transfer channels [34, 35]. As a consequence, superior electrochemical performance can be approached easily.

Figure 3 illustrates the SEM micrographs of MCG aerogels. All foams exhibit continuous and relatively tight three-dimensional (3D) networks and laminated structures. However, the structural integrity of foams with different MXene contents varies. The samples were subjected to freezing in a refrigerator, resulting in the formation of a homogeneous crystal template out of water due to the comparatively slower freezing rate. This in turn gave the samples an isotropic pore structure, which was significantly different from liquid nitrogen results [36, 37]. Figure 3 shows that MCG-0 foam integrity is at its lowest level and the lamellar structure linkage is insufficient, revealing a smooth and flat surface after magnification. At this point, the foam inner structure contains only reduced graphene oxide (rGO) and cellulose nanofibre (CNF) without MXene. Additionally, the FE-SEM elemental mapping in Fig. 3(a) illustrates that carbon and oxygen elements are uniformly distributed throughout the structure and there are no other impurities in the elemental analysis (Fig. S1).

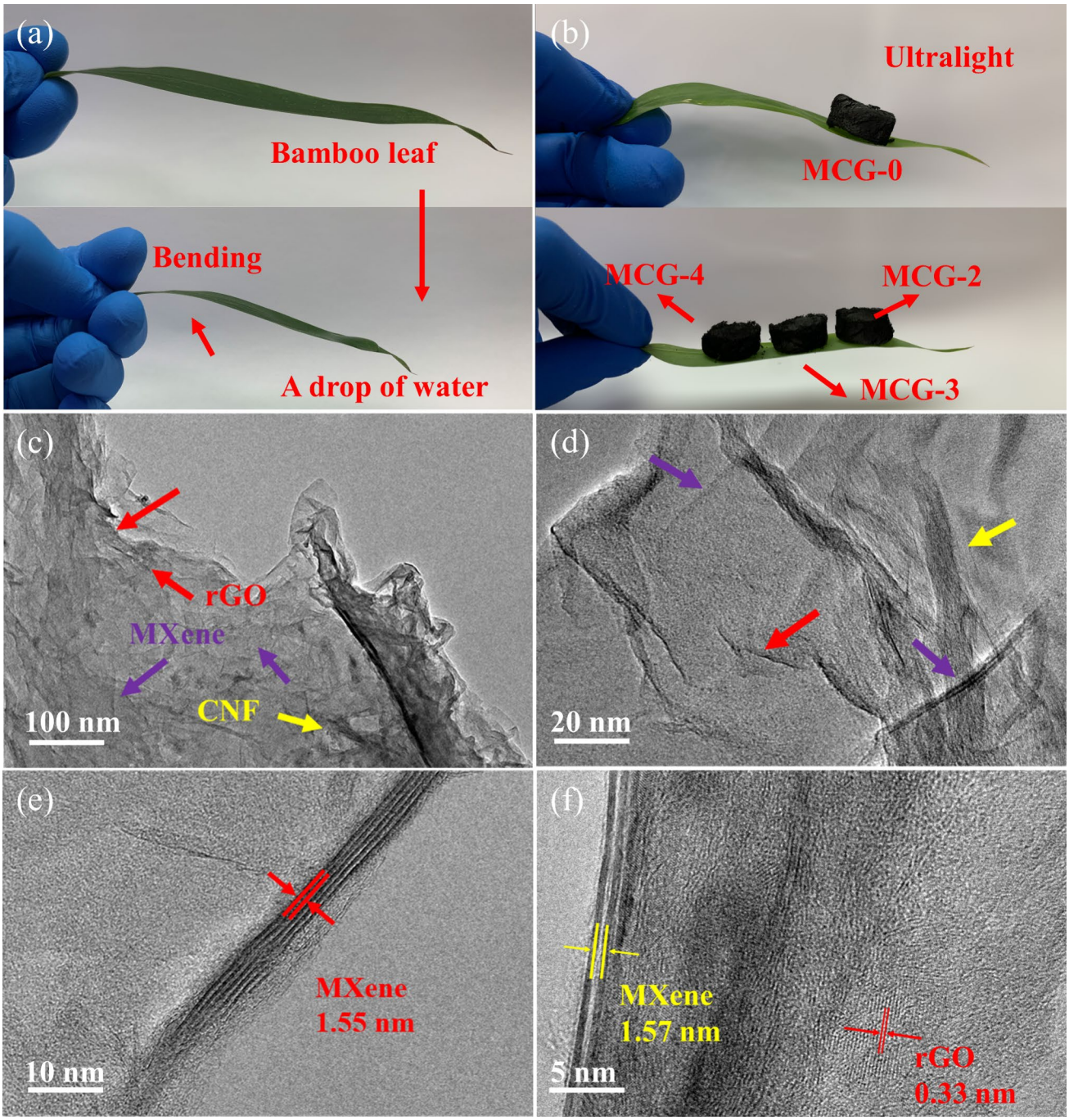

Fig. 2 Structural properties and morphology of the MCG-2 aerogel. **a** A leaf bent by a drop of water and **b** digital photographs of MCG-2. **c**, **d** TEM micrograph of the MCG-2 aerogel. **e**, **f** High-resolution TEM micrographs of the MCG-2 aerogel

In comparison, the network structure of MCG series aerogels appears to be more complex after MXene injection. Figure 3 (d, e), (g, h) and (j, k) demonstrate the FE-SEM micrographs of MCG-2, MCG-3 and MCG-4, respectively, where the previously highly coherent 3D network structure tends to self-stack again due to the increase in the MXene ratio. This situation allows the originally enlarged specific surface area to deteriorate and subsequently complicates the infiltration of electrolytes into electrode surfaces. Therefore, the electrochemical reaction is insufficient and not conducive to electron transfer, which is a devastating circumstance that should be avoided in water-based energy storage system [38]. Moreover, the homogeneous distribution of Ti elements on the energy-dispersive spectroscopy (EDS) patterns of MCG-2

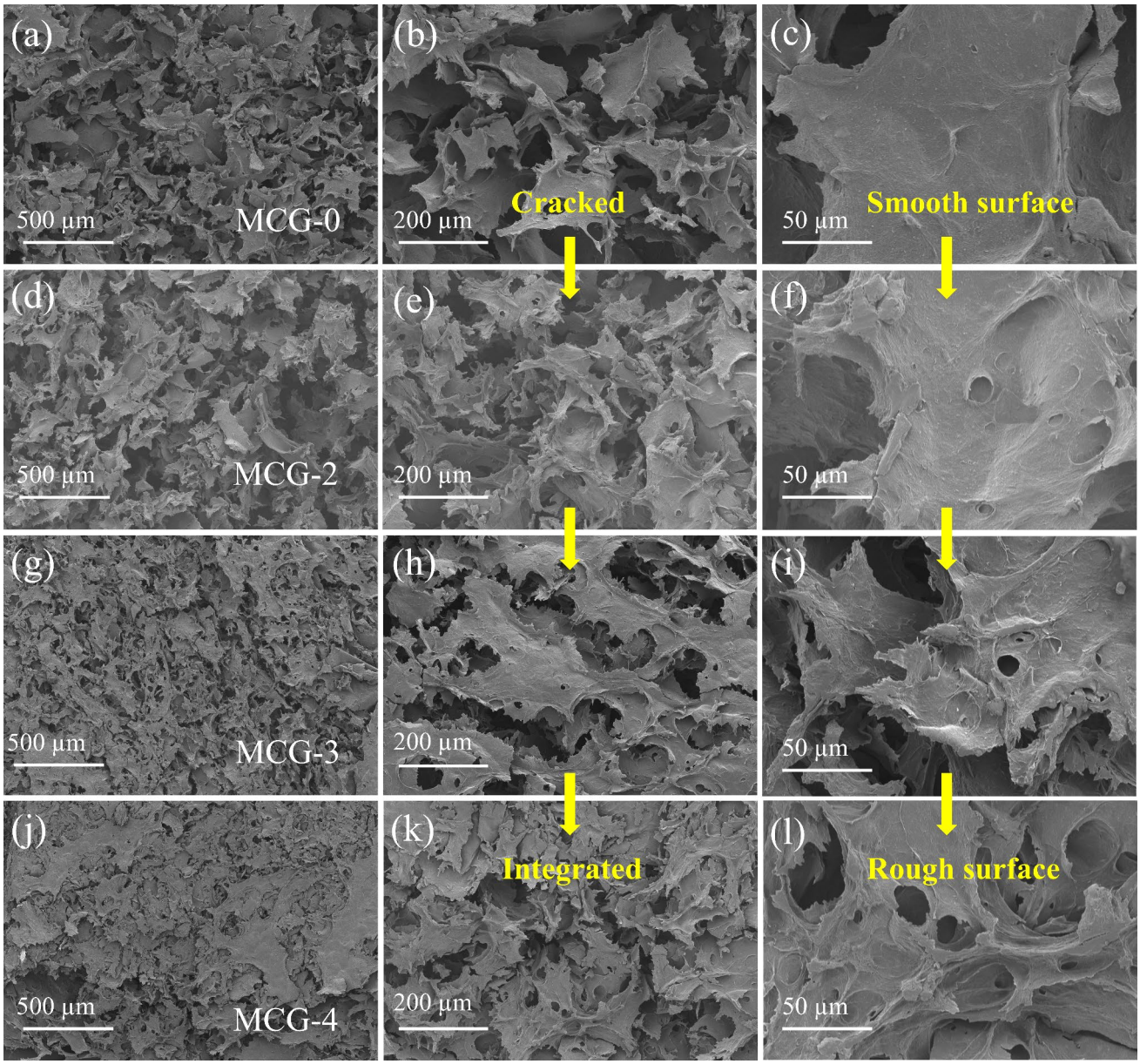

Fig. 3 SEM micrographs of aerogel. (**a–c**) MCG-0 aerogel. (**d–f**) MCG-2 aerogel. (**g–i**) MCG-3 aerogel. (**j–l**) MCG-3 aerogel

aerogels confirms that MXene has been homogeneously compounded with CNF and rGO (Fig. S2). Comparing MCG-4, MCG-3 and MCG-2 aerogels with MCG-0 aerogels, the porous walls of MCG-4, MCG-3 and MCG-2 aerogels were rougher due to the inferior flexibility of MXene compared with rGO. This resulted in greater surface variability for aerogels containing MXene than those without them. In addition, it reduced the aggregation and curling of large graphene nanosheets, indirectly confirming the effective adsorption of MXene onto the rGO layer [39, 40].

The nitrogen isotherms and pore size distribution pattern of MCG foam are illustrated in Fig. 4a and b. It is noteworthy that all MCG aerogels exhibit similar IV isotherms, indicating that the fundamental 3D framework of CNF and rGO aerogels was unaffected by the MXene addition. The samples are primarily composed of macropores and mesopores, which is further supported by the pore size distribution curves that display multiple peaks in the mesopore range. Table S2 provides comprehensive information on the pore parameters of each sample. There is particular interest in the fact that MCG-2 has a maximum surface area of 135.43 m^2g^{-1}, which is substantially greater compared to MCG-0 (65.33 m^2g^{-1}). Additionally, this sample has mesopores and macropores (0.27 cm^3g^{-1}). The relatively extensive specific surface area of MCG-2 contributes sites for the pseudocapacitive redox process at the

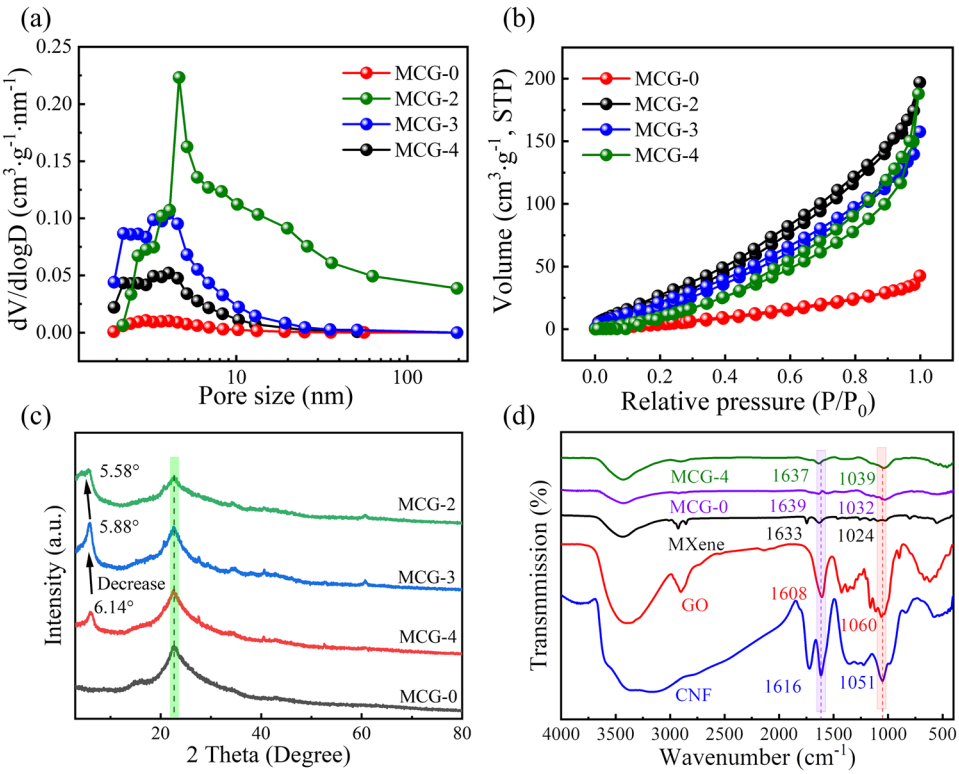

Fig. 4 Microstructure characterisations of the MCG-0, MCG-2, MCG-3 and MCG-4 aerogels. **a** N_2 adsorption/desorption isotherms. **b** Pore size distribution patterns. **c** XRD patterns of MCG aerogel with different content of MXene. **d** FTIR spectra of MCG aerogel with different content of MXene

electrode–electrolyte interface [41]. Conversely, the lower specific surface area of MCG-0 and the decreased specific surface area of MCG-3 and MCG-4 can be attributed to the self-stacking between rGO nanosheets or severe self-stacking between rGO and CNF and MXene, respectively [18].

This study thoroughly examined the phase structure and surface chemistry of MCG aerogels through Fourier transform infrared spectroscopy (FTIR) and X-ray diffractometry (XRD). The XRD findings indicate that the (002) signal peak was significantly present in all samples except for the MCG-0 sample which was free of MXene. Furthermore, all samples showed the characteristic signal peak of rGO ($2\theta = 22.6°$). The presence of the characteristic peak of rGO suggests that VC was an effective reducing agent in the entire hydrothermal reaction [42, 43]. The signal peak of MCG-4 exhibited a significant left shift from $2\theta = 5.58$ to 6.14° compared to that of MCG-2. This indicates that the layer spacing of 2D nanosheets reduced from 1.58 to 1.44 nm. The excessive MXene nanosheets exceeded the threshold of CNF as an intercalating substance between MXene and rGO, thereby causing the self-stacking issue [11]. It is noteworthy that MXene in colloidal solution is prone to oxidation after high temperatures [44]. However, the XRD patterns of all MCG foams in this study did not show distinctive titanium dioxide peaks. This suggests that ascorbic acid plays a significant role in preventing MXene oxidative degradation. It is hypothesised that ascorbic acid in the mixed colloidal solution can create a dense protective layer on the MXene surface to restrain oxidation [45]. From Fig. 4d, the characteristic peaks of CNF appearing at 1051 cm^{-1} and 1616 cm^{-1} are due to the stretching vibrations of the pyranose ring (i.e. C-O and ether bonds) in alkoxy groups [46, 47]. The representative peaks of rGO and CNF also appeared in MCG aerogels, migrating to 1637 cm^{-1} and 1639 cm^{-1}, and 1039 cm^{-1} and 1032 cm^{-1} in MCG-0 and MCG-4 aerogels, respectively. This indicates the outstanding integration of rGO and CNF and the triple bonding between MXene, CNF and rGO [48].

The cross-linking mechanism of hybrid hydrogels, which composed of rGO, MXene, and CNF was studied by means of X-ray photoelectron spectroscopy (XPS). Fig 5a and d present MXene and MCG-2 XPS spectra. The O 1 s and C 1 s signals in MCG-2 were significantly intensified, while the Ti and F elements were weakened. The reduction of GO to rGO has led to increasing C elements. Furthermore, the CNF surface is rich in oxygen-containing functional groups, which provide a substantial amount of O elements. However, the decrease in the proportion of MXene in the hybrid hydrogel is the primary reason for the decrease in the percentage of F 1 s and Ti 2p elements in MCG-2. The C 1 s spectra of MXene can be deconvoluted into five peaks that correspond to Ti-C (281.9 eV), C–C (284.8 eV), C-O (286.2 eV), C = O (287.5 eV) and O-C = O (288.5 eV), respectively. The universal growth of the binding energy of the corresponding characteristic peaks in MCG-2 suggests the outstanding cross-linking of both rGO and CNF with MXene.

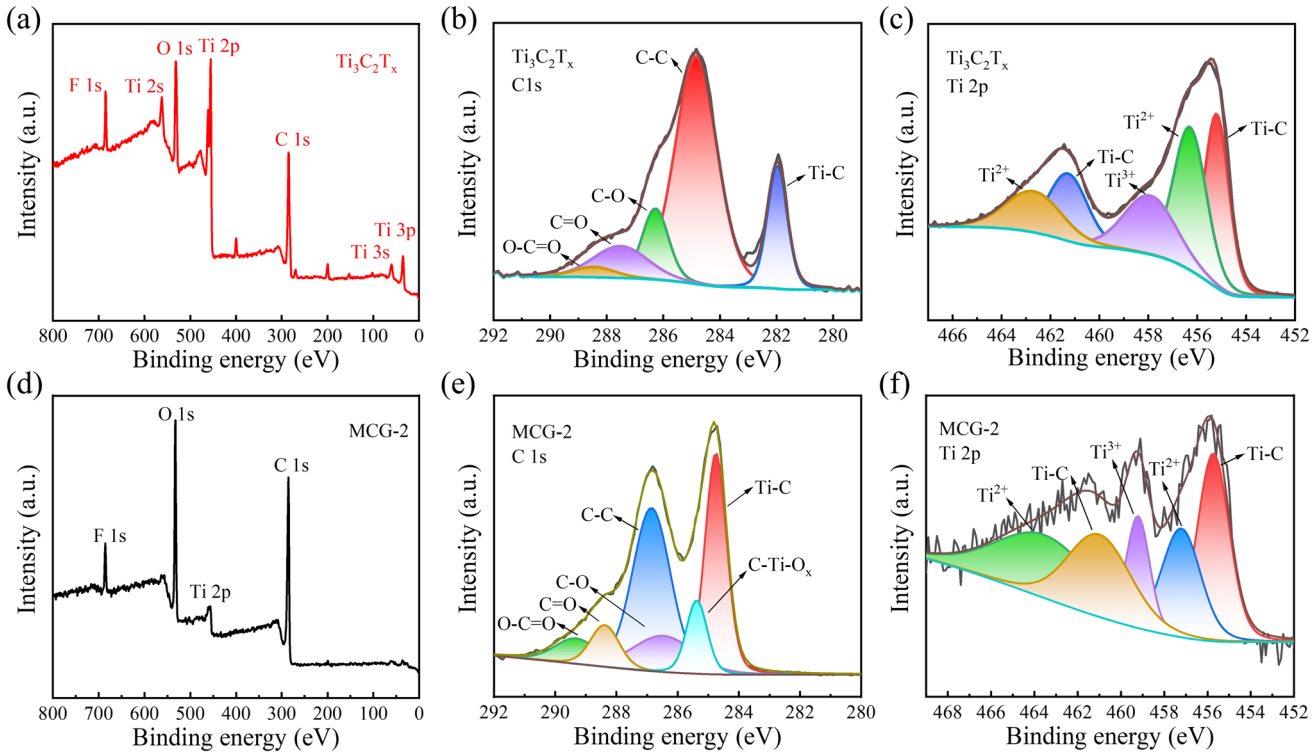

Fig. 5 **a** XPS spectra of MXene. High-resolution XPS spectra of **b** C 1 s and **c** Ti 2p of pristine MXene. **d** XPS spectra of MCG-2. High-resolution XPS spectra of **e** C 1 s and **f** Ti 2p of MCG-2 hybrid aerogel

Additionally, the appearance of C-Ti-O_x (285.4 eV) confirms the possibility of the binding mode of intermediates after the reaction of VC and MXene surface hydroxyl groups. Hydrogen bonds are formed with the hydroxyl group on the CNF surface. However, the Ti 2p spectra of MCG-2 and MXene hardly showed any change in the deconvolution peaks. This indicates that the functional moieties on the MXene surface are well-preserved and do not affect its pseudocapacitive charge storage performance and mechanism [48]. Furthermore, no characteristic TiO_2 peaks were found in the XPS spectra, which demonstrating the excellent inhibitory effect of VC on the MXene oxidation in the hydrothermal reaction. Overall, the XPS analysis provides critical insights into the cross-linking mechanism of MXene, CNF and rGO hybrid hydrogels, which can potentially enhance their performance in various applications.

The above analysis results provide insights into the MCG aerogel reaction process and cross-linking mechanism. As portrayed in Fig. 6, the VC added to the mixed colloidal solution triggers a spontaneous reaction with -OH on the MXene surface which creating a Ti–O-R bonding state. This state effectively protects MXene from oxidation, even they expose to high temperatures (90 °C). And that is the most vital processing for protecting pseudocapacitor provider, $Ti_3C_2T_x$, from losing their capacity contribution. On the surface of the GO, VC reacts with the oxygen-containing terminal groups which leading to the reduction of GO to rGO and the new building of C–O–C bonds. CNF significantly bridges the rGO/VC nanosheets and MXene/VC, forming the 3D macroporous aerogel skeleton framework (MCG). The bonding force between VC, MXene and rGO is significantly weaker during annealing than between VC and CNF, and the high temperature causes VC to disappear during the annealing process. As a result, CNF acting as a binder directly connects the MXene and rGO nanosheets. The precipitation of VC in the final byproduct of the reaction confirms that this process indeed occurred. Therefore, the proposed mechanism highlights the key role played by VC, MXene, GO and CNF in forming MCG aerogel.

3.2 Electrochemical performances of $Ti_3C_2T_x$/CNF/rGO hybrid aerogels free-standing electrode

For investigating the influence of CNF on hybrid aerogel electrodes and evaluating the electrochemical performance of the hybrid aerogel, a study has been conducted on the electrochemical characteristics of MCG-0, MCG-2, MCG-3 and MCG-4 foam electrodes in the three-electrode configuration under 1 M H_2SO_4. The cyclic voltammogram (CV) curves of the various MCG hybrid aerogel electrodes were analysed (Fig. 7a; Fig. S3(a–d)). The area capacitances of MCG-0, MCG-2, MCG-3 and MCG-4 were calculated according to the Eq. (1) at 5 mV s^{-1} (scan rate) (Fig. S3(e)),

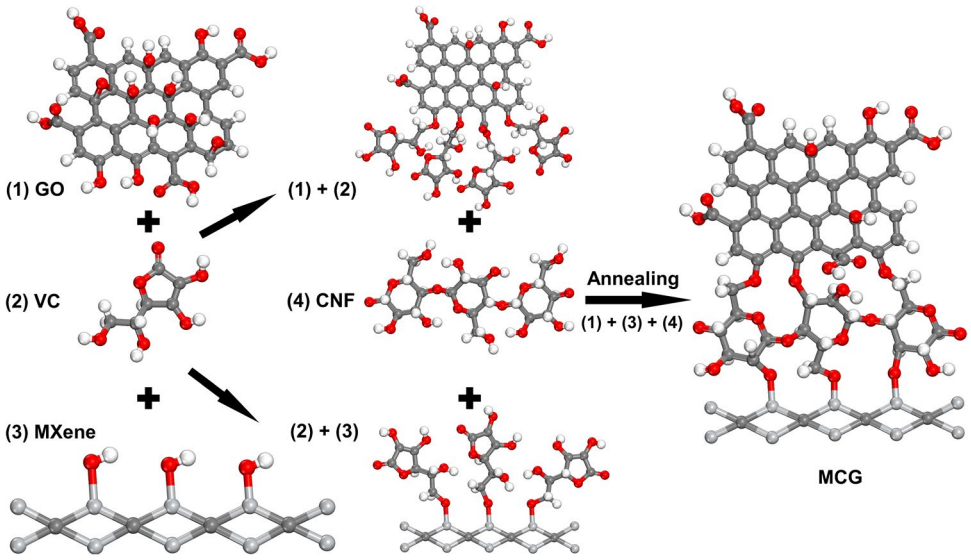

Fig. 6 Diagrammatic representation of the crosslinking process between CNF with GO nanosheets and MXene

and the results (385, 671, 519 and 484 mF·cm^{-2}) indicated that the incorporation of a certain amount of CNF had a favourable effect on modulating the three-dimensional porous framework of the electrode. This led to increased lattice spacing, superior kinetic diffusion of electrolytes and enrichment of the active electrochemical centres. However, the surface reaccumulation caused by excessive 2D nanosheets in MCG-2 and MCG-3 electrodes prevented the electrolyte from fully utilising the electrochemically active centres, leading to low capacitance. Contrarily, the low

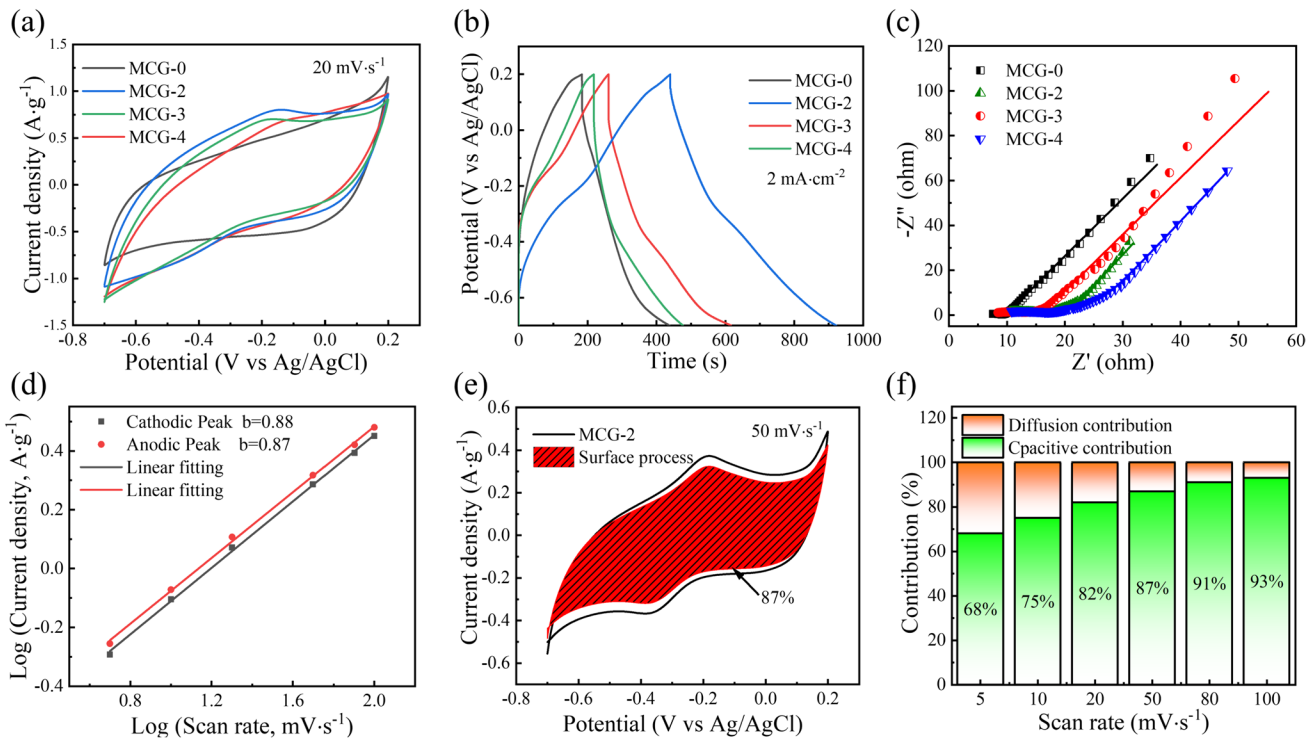

Fig. 7 Three-electrode configuration of MCG electrode in 1 M H_2SO_4. **a** CV curves of MCG-X at 20 mV·s^{-1}. **b** GCD curves of MXene and MCG-X at 2 mA·cm^{-2} current density. **c** MCG-X Nyquist plots represent the equivalent circuit fitting result by a solid line. **d** Logarithm plot of anodic and cathodic peak currents as scan rates function. **e** The surface capacitive contribution is represented by the shadowed area on the CV curves, which were obtained at a rate of 50 mV s^{-1}. **f** The obtained ratio of capacitive contributions was recorded at various scan rates ranging from 5 to 100 mV s^{-1}

capacitance of MCG-0 was mainly attributed to the absence of MXene, which is a surface pseudocapacitance material.

All cyclic voltammetry (CV) curves exhibited two prominent redox peaks (except MCG-0) between − 0.7 and 0.2 V (in comparison to Ag/AgCl), inferring that the energy storage mechanism of the MCG hybrid electrode remained in its original charge-storage system of MXene that uses pseudocapacitance. However, the changes in functional groups on the MXene surface could explain the shift in peak position. The MXene addition substantially improved the capacitance of MCG-0 by modifying its double-layer charge storage mechanism. A galvanostatic charge–discharge (GCD) curve was analysed for each electrode and showed no distinct potential platform, indicating that both double-layer capacitance and pseudocapacitance were devoted to the capacitance. The charging-discharging curves of each electrode at various current densities exhibited high symmetry triangles, which is a typical feature of pseudocapacitive behaviour. This observation suggests that the electrode coulombic efficiency was high and the surface redox reaction was highly reversible. Notably, the MCG-2 electrode demonstrated impressive rate performance, displaying a capacitance of 352 mF cm^{-2} (52.5%) at 100 mV s^{-1}. This was significantly higher than that of MCG-0, MCNF-3 and MCNF-4, which displayed capacitances of 162 mF cm^{-2} (42.1%), 239 mF cm^{-2} (46.1%) and 224 mF cm^{-2} (46.3%), respectively (Fig. S3(e) and (f)).

Electrochemical impedance spectra (EIS) are a valuable tool for analysing the capacitance changes in electrochemical kinetics and resistance of different electrodes. The intercept on the real axis in the high-frequency region indicates either the internal resistance or the equivalent series resistance (Rs). According to Fig. 7c, the values of Rs for MCG-0, MCG-2, MCG-3 and MCG-4 electrodes are 7.0, 7.2, 7.9 and 8.2 Ω, respectively. It is noteworthy that the internal resistance of the MCG aerogel containing MXene is slightly increased due to the influence of the insulating properties of CNF, which explains the reduced gravitative capacitance of the hybrid aerogel. However, the aerogel electrode displays comparable lines to the MXene-free electrode in the low-frequency region, inferring superior capacitive performance and ion diffusion. By fitting the equivalent circuit diagram, the charge transfer resistance (Rct) of the MCG-2 electrode (Rct = 7.5 Ω) was calculated and was found to be reduced compared to MCG-0 (Rct = 8.7 Ω). This decrease in Rct was attributed to superior electroactive specific surface area and conductivity [49]. These findings suggest that the 3D macroporous skeleton structure has a negligible impact on the enhanced interface contact within the electrode and electrolyte.

By examining the power law relationship among the CV peak current (i) and the scan rate (V) with a specific equation, the charge storage mechanism of the MCG-2 electrode can be investigated as follows:

$$i = av^b \tag{7}$$

when adjusting the parameters a and b, a straight line can be created by mapping $\log(i)$ to $\log(v)$. The value of b represents the slope of this line. When b equals 1, the surface capacity governs the charge storage kinetics. Conversely, when b equals 0.5, the charge storage kinetics is dominated by diffusion. Figure 7 d illustrates that the cathodic and anodic peaks for the MCG-2 electrode exhibit slopes of 0.88 and 0.87, respectively. The capacitive surface process is the main charge storage mechanism in this context. To evaluate the capacitive behaviour and diffusion-controlled process contribution, the following relationship was used at different scan rates:

$$i = k_1 v + k_2 v^{1/2} \tag{8}$$

where $k_2 v^{1/2}$ and $k_1 v$ denote the diffusion contribution and fraction of capacitive contribution, respectively. At a scan rate of 50 mV s^{-1}, the shaded area in Fig. 7e represents approximately 87% of the capacitance contribution. However, the capacitance contribution increases to 93% when the scan rate is raised to 100 mV s^{-1} (Fig. 7f). It is imperative to examine the underlying factors that explain the predominance of Faradaic pseudocapacitive behaviour as the primary mode of charge storage. Firstly, the electrodes themselves are fabricated from materials with remarkable electronic conductivity. Secondly, the 3D macroporous network architecture of these electrodes facilitates hydrogen ion diffusion into the active material's surface structure [50, 51].

3.3 Electrochemical performance of the MCG-2 symmetric supercapacitor

An examination of MCG-2 electrodes was conducted to assess the practical application potential of MCG aerogel electrodes. These electrodes were selected based on prior electrochemical analysis, and they were assembled as symmetrical supercapacitors to evaluate their effectiveness. The CV curves of the symmetrical device were tested in the 0–1.0-V voltage at 5 to 100 mV s^{-1}. The findings in Fig. 8a indicate a stable curve shape without significant polarisation phenomena. Furthermore, the curve remained unchanged at 100 mV s^{-1}, which demonstrates the exceptional rate capability of the device. The CV curve at a scan rate of 5 mV s^{-1} reveals a pair of distinct broad redox peaks, indicating the pseudocapacitive behaviour of the device. The GCD curve showed similar results (Fig. 8c), which displayed a nearly symmetrical triangle with no significant voltage drop that demonstrated typical pseudocapacitance characteristics.

Figure 8b presents the EIS measurement results of the device, while the equivalent circuit diagram of the

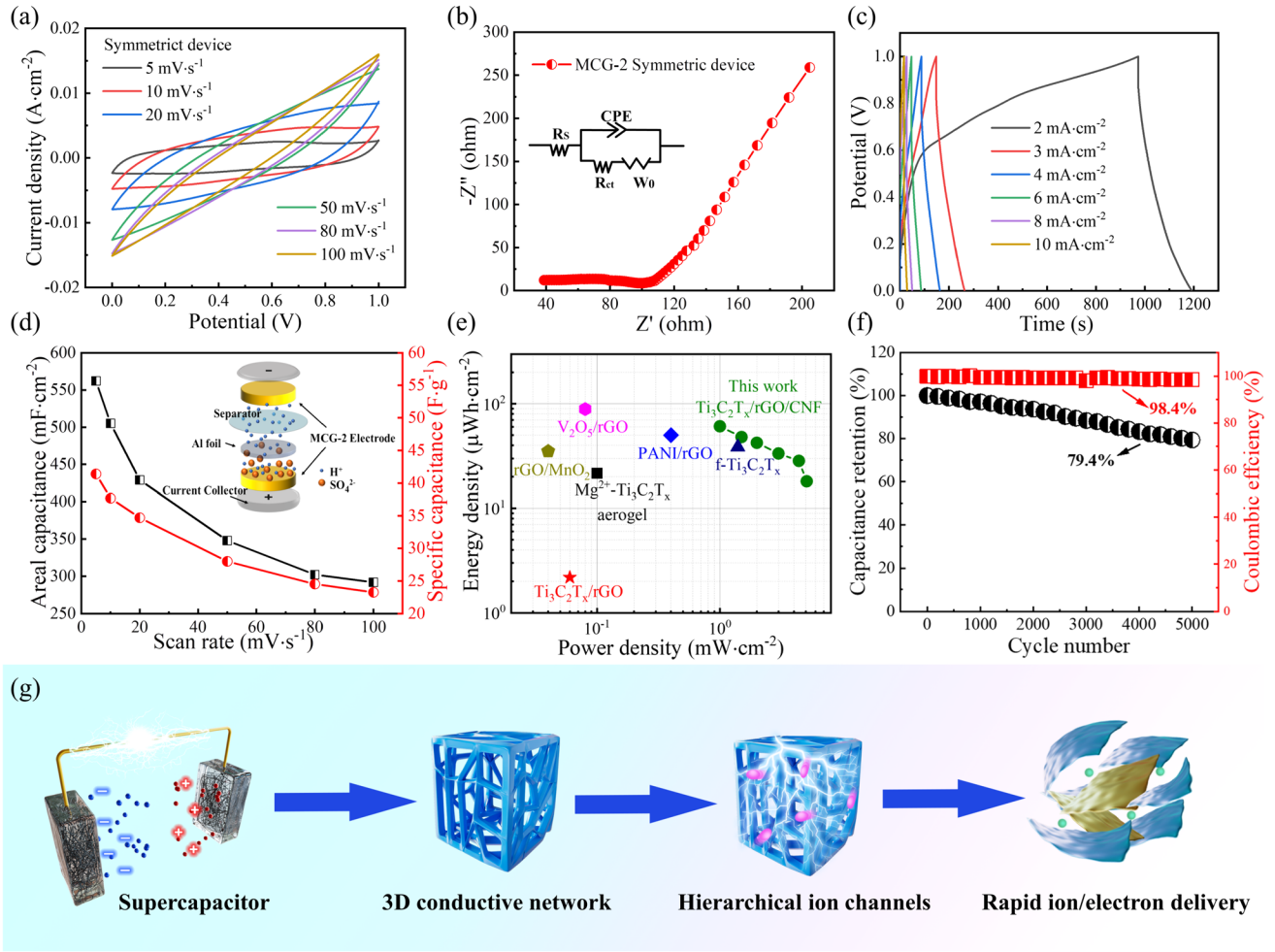

Fig. 8 **a** Various scan rates ranging from 5 to 100 mV s^{-1} were used to obtain CV profiles between 0 and 1.0 V. **b** The Nyquist plot for the symmetric supercapacitor is displayed with an inset featuring the electrical equivalent circuit model for the plot. **c** GCD profile measured at current densities between 1 and 20 mA cm^{-2}. **d** Gravimetric capacitance and areal capacitance based on the MCG-2 aerogel electrodes at 5 to 100 mV·s^{-1}. Inset shows the structure of the assembled symmetrical supercapacitor. **e** Comparison of the MCG-2//MCG-2 symmetric supercapacitor to other supercapacitors using Ragone plots. **f** Cycling efficiency of the symmetric supercapacitor device was quantified at 20 mA·cm^{-2}. **g** Illustration shows the roles of the hierarchical inner structure of MCG aerogel

symmetrical device is displayed in the inset. The significantly large slope of the Nyquist curve in the low-frequency region indicates the ideal ion diffusion behaviour. On the other hand, the small X-axis intercept and favourable semicircle diameter in the high-frequency region demonstrate the small resistance of charge transfer and equivalent series of the device. Figure 8d presents the results of calculating the areal specific capacitance of the MCG-2 symmetric device at various scan rates. The assembled symmetric supercapacitor structure is shown in the inset. The device exhibited a specific capacity of 562 mF cm^{-2} (41 F g^{-1}) at a scan rate of 5 mV s^{-1} and 292 mF cm^{-2} (23 F g^{-1}) at 100 mV s^{-1}, which is indicative of its exceptional rate capability.

The Ragone plots provide a graphical representation of the power and energy density of a device, and they illustrate the impressive electrochemical performance of MCG symmetric supercapacitors. These supercapacitors exhibit a remarkable energy density of 60.9 μWh·cm^{-2} at 1.0 mW cm^{-2}. Moreover, they maintain a high energy density of 18.1 μWh cm^{-2} even when the power density surges to 5.1 mW cm^{-2}, thereby demonstrating their exceptional rate capability (Fig. 8e). Notably, the MCG-2 symmetric supercapacitors surpass the recently announced MXene or rGO-based symmetric supercapacitors in terms of performance. Moreover, the energy density achieved by MCG-2 symmetric supercapacitors surpasses several formerly identified rGO- or MXene-based supercapacitors, such as MoS_2/rGO/CNF (45.7 μWh·cm^{-2}, 8.56 mW·cm^{-2}) [52], PPy/rGO/CNF (60.5 μWh·cm^{-2}, 0.10 mW·cm^{-2}) [53], Ti_3C_2/f-CNCs (38.5 μWh·cm^{-2}, 1.40 mW·cm^{-2}) [25], rGO/MnO_2 (35.1 μWh·cm^{-2}, 0.04 mW·cm^{-2}) [54], and CNC/rGO/CNF (31.25 μWh·cm^{-2}, 1.50 mW·cm^{-2}) [55] (Table S3).

MCG-2 symmetric supercapacitors demonstrate exceptional cycling stability, preserving 79.4% of their initial capacitance after 5000 consecutive charge/discharge cycles at 20 mA cm^{-2} (Fig. 8f). MCG electrodes demonstrate superior electrochemical performance including specific capacity and energy density because of their efficient utilisation of space in the electrode, which includes a hierarchical ion channel structure that allows rapid ion diffusion. Furthermore, the additional double-layer capacitance contribution of the rGO compensates for the insufficient operating potential window of the pure MXene device, resulting in a higher energy density (Fig. 8g). In terms of practical application, the binder-free electrode not only saves economic costs but also realises light-weight devices. The utilisation of environmental friendly materials, like cellulose nanofibres, and easily achievable methods, like low-temperature hydrothermal and freeze-drying, all demonstrate sustainable fabrication concept, which are well consistent with the zero carbon emission policy in the world. To sum up, the MCG-2 symmetric device boasts impressive electrochemical performance and a well-thought-out electrode structure. This makes it a highly reliable and powerful energy storage solution that could be adopted in various emerging and potential contexts [56, 57].

4 Conclusions

This study demonstrates the successful development of hybrid aerogels that are interconnected and three-dimensional via the integration of freeze-drying and hydrothermal methods. The process entails the application of highly conductive 2D nanosheets of MXene and GO, which serve as the primary capacitive contributor and charge-conducting material. In addition, we utilised cellulose nanofibres, a sustainable green material, to act as a "bridge" for hydrogen bonding on the two nanosheets surface, and VC acts as both an oxidation-resistant agent for MXene and a reductant for GO. In the three-electrode system (5 mV s^{-1}), the MCG-2 electrode yielded an optimum areal capacitance of 671 mF cm^{-2} in 1 M H_2SO_4 aqueous solution. The capacitance remained at 352 mF cm^{-2} even when increasing the current density to 100 mV s^{-1}, resulting in a retention rate of 52.5%. At 1.0 mW cm^{-2} power density, our assembled devices showcase a high energy density of 60.9 μWh·cm^{-2} and a voltage of 1.0 V in the H_2SO_4 electrolyte. The symmetric device demonstrated excellent electrochemical stability, maintaining a superior capacitance retention of 79.4% at 20 mA cm^{-2} current density. This study offers an encouraging opportunity to investigate any possible changes in the material internal structure that may affect its overall performance and functionalised utilisation.

Supplementary Information The online version contains supplementary material available at https://doi.org/10.1007/s42114-024-00877-8.

Acknowledgements The support provided by the Advanced Analysis and Testing Center of Nanjing Forestry University is gratefully acknowledged by the authors.

Author contributions Xiaoyu Bi and Yang Shi wrote the main manuscript text. Xiaoyu Bi and Yang Shi prepared all the figures. Shengbo Ge, Ben Bin Xu and Ximin He edited the main manuscript text. Shengbo Ge, Xia Li and Runzhou Huang revised and supported funding. All authors reviewed the manuscript.

Funding This work was supported by the National Natural Science Foundation of China (32201491, 32101444), the Young Elite Scientists Sponsorship Program by CAST (2023QNRC001), the Major Projects of Natural Science Foundation of Jiangsu (18KJA220002), and the Special Program of the China Postdoctoral Science Foundation (2017T100313).

Data availability The data presented in this study are available on request from the corresponding author.

Declarations

Competing interests The authors declare no competing interests.

References

1. Fan G, Wang Z, Ren H, Liu Y, Fan R (2021) Dielectric dispersion of copper/rutile cermets: dielectric resonance, relaxation, and plasma oscillation. Scripta Mater 190:1–6. https://doi.org/10.1016/j.scriptamat.2020.08.027
2. Gogotsi Y, Simon P (2011) True performance metrics in electrochemical energy storage. Science 6058:917–918. https://doi.org/10.1126/science.1213003
3. Lu X, Yu M, Wang G, Tong Y, Li Y (2014) Flexible solid-state supercapacitors: design, fabrication and applications. Energy Environ Sci 7:2160–2181. https://doi.org/10.1039/c4ee00960f
4. Yuan H, Wang G, Zhao Y, Liu Y, Wu Y, Zhang Y (2020) A stretchable, asymmetric, coaxial fiber-shaped supercapacitor for wearable electronics. Nano Res 6:1686–1692. https://doi.org/10.1007/s12274-020-2793-x
5. Zhang J, Seyedin S, Gu Z, Yang W, Wang X, Razal JM (2017) MXene: a potential candidate for yarn supercapacitors. Nanoscale 47:18604–18608. https://doi.org/10.1039/c7nr06619h
6. Shekhirev M, Shuck CE, Sarycheva A, Gogotsi Y (2021) Characterization of MXenes at every step, from their precursors to single flakes and assembled films. Prog Mater Sci 120:100757. https://doi.org/10.1016/j.pmatsci.2020.100757
7. Hantanasirisakul K, Gogotsi Y (2018) Electronic and optical properties of 2D transition metal carbides and nitrides (MXenes). Adv Mater 52:1804779. https://doi.org/10.1002/adma.201804779
8. Cao WT, Chen FF, Zhu YJ, Zhang YG, Jiang YY, Ma MG, Chen F (2018) Binary strengthening and toughening of MXene/cellulose nanofiber composite paper with nacre-inspired structure and superior electromagnetic interference shielding properties. ACS Nano 5:4583–4593. https://doi.org/10.1021/acsnano.8b00997
9. Li K, Liang M, Wang H, Wang X, Huang Y, Coelho J, Pinilla S, Zhang Y, Qi F, Nicolosi V, Xu Y (2020) 3D MXene architectures for efficient energy storage and conversion. Adv Funct Mater 47:2000842. https://doi.org/10.1002/adfm.202000842
10. Pang J, Mendes RG, Bachmatiuk A, Zhao L, Ta HQ, Gemming T, Liu H, Liu Z, Rummeli MH (2019) Applications of 2D MXenes in

energy conversion and storage systems. Chem Soc Rev 1:72–133. https://doi.org/10.1039/c8cs00324f
11. Shang T, Lin Z, Qi C, Liu X, Li P, Tao Y, Wu Z, Li D, Simon P, Yang QH (2019) 3D macroscopic architectures from self-assembled MXene hydrogels. Adv Funct Mater 33:1903960. https://doi.org/10.1002/adfm.201903960
12. Pang D, Alhabeb M, Mu X, Dall'Agnese Y, Gogotsi Y, Gao Y (2019) Electrochemical actuators based on two-dimensional Ti3C2Tx (MXene). Nano Lett 10:7443–7448. https://doi.org/10.1021/acs.nanolett.9b03147
13. Xie P, Zhang Z, Liu K, Qian L, Dang F, Liu Y, Fan R, Wang X, Dou S (2017) C/SiO2 meta-composite: overcoming the λ/a relationship limitation in metamaterials. Carbon 125:1–8. https://doi.org/10.1016/j.carbon.2017.09.021
14. Zhang Z, Chi K, Xiao F, Wang S (2015) Advanced solid-state asymmetric supercapacitors based on 3D graphene/MnO2 and graphene/polypyrrole hybrid architectures. J Mater Chem A 24:12828–12835. https://doi.org/10.1039/c5ta02685g
15. Cao X, Yin Z, Zhang H (2014) Three-dimensional graphene materials: preparation, structures and application in supercapacitors. Energy Environ Sci 6:1850–1865. https://doi.org/10.1039/c4ee00050a
16. Xie X, Zhao MQ, Anasori B, Maleski K, Ren CE, Li J, Byles BW, Pomerantseva E, Wang G, Gogotsi Y (2016) Porous heterostructured MXene/carbon nanotube composite paper with high volumetric capacity for sodium-based energy storage devices. Nano Energy 26:513–523. https://doi.org/10.1016/j.nanoen.2016.06.005
17. Du YT, Kan X, Yang F, Gan LY, Schwingenschlogl U (2018) MXene/graphene heterostructures as high-performance electrodes for Li-ion batteries. ACS Appl Mater Interfaces 38:32867–32873. https://doi.org/10.1021/acsami.8b10729
18. Chen W, Zhang D, Yang K, Luo M, Yang P, Zhou X (2021) Mxene ($Ti_3C_2T_x$)/cellulose nanofiber/porous carbon film as free-standing electrode for ultrathin and flexible supercapacitors. Chem Eng J 413:127524. https://doi.org/10.1016/j.cej.2020.127524
19. Dreyer DR, Park S, Bielawski CW, Ruoff RS (2010) The chemistry of graphene oxide. Chem Soc Rev 1:228–240. https://doi.org/10.1039/b917103g
20. Zhu Y, Murali S, Cai W, Li X, Suk JW, Potts JR, Ruoff RS (2010) Graphene and graphene oxide: synthesis, properties, and applications. Adv Mater 35:3906–3924. https://doi.org/10.1002/adma.201001068
21. Shao L, Xu J, Ma J, Zhai B, Li Y, Xu R, Ma Z, Zhang G, Wang C, Qiu J (2020) MXene/RGO composite aerogels with light and high-strength for supercapacitor electrode materials. Compos Commun 19:108–113. https://doi.org/10.1016/j.coco.2020.03.006
22. Xu T, Du H, Liu H, Liu W, Zhang X, Si C, Liu P, Zhang K (2021) Advanced nanocellulose-based composites for flexible functional energy storage devices. Adv Mater 48:2101368. https://doi.org/10.1002/adma.202101368
23. Chen W, Yu H, Lee SY, Wei T, Li J, Fan Z (2018) Nanocellulose: a promising nanomaterial for advanced electrochemical energy storage. Chem Soc Rev 8:2837–2872. https://doi.org/10.1039/c7cs00790f
24. Yang X, Yao Y, Wang Q, Zhu K, Ye K, Wang G, Cao D, Yan J (2022) 3D macroporous oxidation-resistant $Ti_3C_2T_x$ MXene hybrid hydrogels for enhanced supercapacitive performances with ultralong cycle life. Adv Funct Mater 10:2109479. https://doi.org/10.1002/adfm.202109479
25. Cai C, Wei Z, Deng L, Fu Y (2021) Temperature-invariant superelastic multifunctional MXene aerogels for high-performance photoresponsive supercapacitors and wearable strain sensors. ACS Appl Mater Interfaces 45:54170–54184. https://doi.org/10.1021/acsami.1c16318
26. Chen WY, Lai SN, Yen CC, Jiang X, Peroulis D, Stanciu LA (2020) Surface functionalization of $Ti_3C_2T_x$ MXene with highly reliable superhydrophobic protection for volatile organic compounds sensing. ACS Nano 9:11490–11501. https://doi.org/10.1021/acsnano.0c03896
27. Kim J, Yoon Y, Kim SK, Park S, Song W, Myung S, Jung HK, Lee SS, Yoon DH, An KS (2021) Chemically stabilized and functionalized 2D-MXene with deep eutectic solvents as versatile dispersion medium. Adv Funct Mater 13:2008722. https://doi.org/10.1002/adfm.202008722
28. Lin Z, Li X, Zhang H, Xu BB, Wasnik P, Li H, Singh MV, Ma Y, Li T, Guo Z (2023) Research progress of MXenes and layered double hydroxides for supercapacitors. Inorg Chem Front 15:4358–4392. https://doi.org/10.1039/d3qi00819c
29. Yuan G, Wan T, BaQais A, Mu Y, Cui D, Amin MA, Li X, Xu BB, Zhu X, Algadi H, Li H, Wasnik P, Lu N, Guo Z, Wei H, Cheng B (2023) Boron and fluorine Co-doped laser-induced graphene towards high-performance micro-supercapacitors. Carbon 212:118101. https://doi.org/10.1016/j.carbon.2023.118101
30. Fan W, Wang Q, Rong K, Shi Y, Peng W, Li H, Guo Z, Xu BB, Hou H, Algadi H, Ge S (2024) MXene enhanced 3D needled waste denim felt for high-performance flexible supercapacitors. Nano-Micro Lett 16:36. https://doi.org/10.1007/s40820-023-01226-y
31. Cheng Y, Zhu W, Lu X, Wang C (2022) Lightweight and flexible MXene/carboxymethyl cellulose aerogel for electromagnetic shielding, energy harvest and self-powered sensing. Nano Energy 98:107229. https://doi.org/10.1016/j.nanoen.2022.107229
32. Yang X, Wang Q, Zhu K, Ye K, Wang G, Cao D, Yan J (2021) 3D porous oxidation-resistant MXene/Graphene architectures induced by in situ zinc template toward high-performance supercapacitors. Adv Funct Mater 20:2101087. https://doi.org/10.1002/adfm.202101087
33. Yan J, Ren CE, Maleski K, Hatter CB, Anasori B, Urbankowski P, Sarycheva A, Gogotsi Y (2017) Flexible MXene/graphene films for ultrafast supercapacitors with outstanding volumetric capacitance. Adv Funct Mater 30:1701264. https://doi.org/10.1002/adfm.201701264
34. Deng Y, Shang T, Wu Z, Tao Y, Luo C, Liang J, Han D, Lyu R, Qi C, Lv W, Kang F, Yang QH (2019) Fast gelation of $Ti_3C_2T_x$ MXene initiated by metal ions. Adv Mater 43:1902432. https://doi.org/10.1002/adma.201902432
35. Zhao MQ, Ren CE, Ling Z, Lukatskaya MR, Zhang C, Van Aken KL, Barsoum MW, Gogotsi Y (2015) Flexible MXene/carbon nanotube composite paper with high volumetric capacitance. Adv Mater 2:339–345. https://doi.org/10.1002/adma.201404140
36. Gao HL, Zhu YB, Mao LB, Wang FC, Luo XS, Liu YY, Lu Y, Pan Z, Ge J, Shen W, Zheng YR, Xu L, Wang LJ, Xu WH, Wu HA, Yu SH (2016) Super-elastic and fatigue resistant carbon material with lamellar multi-arch microstructure. Nat Commun 7:12920. https://doi.org/10.1038/ncomms12920
37. Bai H, Chen Y, Delattre B, Tomsia AP, Ritchie RO (2015) Bioinspired large-scale aligned porous materials assembled with dual temperature gradients. Sci Adv 11:1500849. https://doi.org/10.1126/sciadv.1500849
38. Dall'Agnese Y, Lukatskaya MR, Cook KM, Taberna PL, Gogotsi Y, Simon P (2014) High capacitance of surface-modified 2D titanium carbide in acidic electrolyte. Electrochem Commun 48:118–122. https://doi.org/10.1016/j.elecom.2014.09.002
39. Ma L, Zhao T, Xu F, You T, Zhang X (2021) A dual utilization strategy of lignosulfonate for MXene asymmetric supercapacitor with high area energy density. Chem Eng J 405:126694. https://doi.org/10.1016/j.cej.2020.126694
40. Fan Z, Wang D, Yuan Y, Wang Y, Cheng Z, Liu Y, Xie Z (2020) A lightweight and conductive MXene/graphene hybrid foam for superior electromagnetic interference shielding. Chem Eng J 381:122696. https://doi.org/10.1016/j.cej.2019.122696
41. Liu T, Zhang F, Song Y, Li Y (2017) Revitalizing carbon supercapacitor electrodes with hierarchical porous structures. J Mater Chem A 34:17705–17733. https://doi.org/10.1039/c7ta05646j
42. Ma Y, Yue Y, Zhang H, Cheng F, Zhao W, Rao J, Luo S, Wang J, Jiang X, Liu Z, Liu N, Gao Y (2018) 3D synergistical MXene/

reduced graphene oxide aerogel for a piezoresistive sensor. ACS Nano 4:3209–3216. https://doi.org/10.1021/acsnano.7b06909
43. Zhao S, Zhang HB, Luo JQ, Wang QW, Xu B, Hong S, Yu ZZ (2018) Highly electrically conductive three-dimensional $Ti_3C_2T_X$ MXene/reduced graphene oxide hybrid aerogels with excellent electromagnetic interference shielding performances. ACS Nano 11:11193–11202. https://doi.org/10.1021/acsnano.8b05739
44. Lotfi R, Naguib M, Yilmaz DE, Nanda J, van Duin ACT (2018) A comparative study on the oxidation of two-dimensional Ti_3C_2 MXene structures in different environments. J Mater Chem A 26:12733–12743. https://doi.org/10.1039/c8ta01468j
45. Zhao X, Vashisth A, Prehn E, Sun W, Shah S, Habib T, Chen Y, Tan Z, Lutkenhaus J, Radovic M, Green MJ (2019) Antioxidants unlock shelf-stable $Ti_3C_2T_X$ (MXene) nanosheet dispersions. Matter 2:513–526. https://doi.org/10.1016/j.matt.2019.05.020
46. Hussain A, Li J, Wang J, Xue F, Chen Y, Bin Aftab T, Li D (2018) Hybrid monolith of graphene/TEMPO-oxidized cellulose nanofiber as mechanically robust, highly functional, and recyclable adsorbent of methylene blue dye. J Nanomater 2018:5963982. https://doi.org/10.1155/2018/5963982
47. Maiti S, Jayaramudu J, Das K, Reddy SM, Sadiku R, Ray SS, Liu D (2013) Preparation and characterization of nano-cellulose with new shape from different precursor. Carbohydr Polym 1:562–567. https://doi.org/10.1016/j.carbpol.2013.06.029
48. Liu YE, Zhang MG, Gao YN, Guo J (2022) Regulate the reaction kinetic rate of lithium-sulfur battery by rational designing of TEMPO-oxidized cellulose nanofibers/rGO porous aerogel with monolayer MXene coating. J Alloys Compd 898:162821. https://doi.org/10.1016/j.jallcom.2021.162821
49. Wang M, Jin F, Zhang X, Wang J, Huang S, Zhang X, Mu S, Zhao Y, Zhao Y (2017) Multihierarchical structure of hybridized phosphates anchored on reduced graphene oxide for high power hybrid energy storage devices. Acs Sustain Chem Eng 7:5679–5685. https://doi.org/10.1021/acssuschemeng.7b00131
50. Brousse T, Belanger D, Long JW (2015) To be or not to be pseudocapacitive ? J Electrochem Soc 5:A5185–A5189. https://doi.org/10.1149/2.0201505jes
51. Fleischmann S, Mitchell JB, Wang R, Zhan C, Jiang DE, Presser V, Augustyn V (2020) Pseudocapacitance: from fundamental understanding to high power energy storage materials. Chem Rev 14:6738–6782. https://doi.org/10.1021/acs.chemrev.0c00170
52. Lv Y, Li L, Zhou Y, Yu M, Wang J, Liu J, Zhou J, Fan Z, Shao Z (2017) A cellulose-based hybrid 2D material aerogel for a flexible all-solid-state supercapacitor with high specific capacitance. Rsc Adv 69:43512–43520. https://doi.org/10.1021/10.1039/c7ra07908g
53. Zhang Y, Shang Z, Shen M, Chowdhury SP, Ignaszak A, Sun S, Ni Y (2019) Cellulose nanofibers/reduced graphene oxide/polypyrrole aerogel electrodes for high-capacitance flexible all-solid-state supercapacitors. Acs Sustain Chem Eng 13:11175–11185. https://doi.org/10.1021/acssuschemeng.9b00321
54. Sumboja A, Foo CY, Wang X, Lee PS (2013) Large areal mass, flexible and free-standing reduced graphene oxide/manganese dioxide paper for asymmetric supercapacitor device. Adv Mater 20:2809–2815. https://doi.org/10.1002/adma.201205064
55. Guo Y, Huang H, Zhao Y, Li C, Cong T, Zhang H, Wen N, Fan Z, Pan L (2022) Collaboratively intercalated 1D/3D carbon nanoarchitectures in rGO-based aerogel for supercapacitor electrodes with superior capacitance retention. Appl Surf Sci 596:153566. https://doi.org/10.1016/j.apsusc.2022.153566
56. Hao Y, Leng Z, Yu C, Xie P, Zhou L, Li Y, Liang G, Li X, Liu C (2023) Ultra-lightweight hollow bowl-like carbon as microwave absorber owning broad band and low filler loading. Carbon 212:118156. https://doi.org/10.1016/j.carbon.2023.118156
57. Fan G, Wang Z, Sun K, Liu Y, Fan R (2021) Doped ceramics of indium oxides for negative permittivity materials in MHz-kHz frequency regions. J Mater Sci Technol 61:125–131